Prostate contours delineation using interactive directional active contours model and parametric shape prior model

Foued Derraz, Gérard Forzy, Arnaud Delebarre, Abdelmalik Taleb-Ahmed, Mourad Oussalah, Laurent Peyrodie, Sebastien Verclytte

Int. J. Numer. Meth. Biomed. Engng. 31/11 (2015)

Prostate contours delineation using interactive directional active contours model and parametric shape prior model

Foued Derraz[1,2,3,5,*,†], Gérard Forzy[3,4], Arnaud Delebarre[4], Abdelmalik Taleb-Ahmed[2,5], Mourad Oussalah[6], Laurent Peyrodie[2,7] and Sebastien Verclytte[4]

[1]*Telecommunications Laboratory, Technology Faculty, Abou Bekr Belkaïd University, Tlemcen, 13000, Algeria*
[2]*Université Nord de France, F-59000 Lille, France*
[3]*Unité de Traitement de Signaux Biomédicaux, Faculté de médecine et maïeutique, Lille, France*
[4]*Groupement des Hopitaux de l'Ínstitut Catholique de Lille, France*
[5]*LAMIH UMR CNRS 8201, Le Mont Houy, Université de Valenciennes et Cambresis, 59313 Valenciennes, France*
[6]*School of Electronics, Electrical and Computer Engineering, University of Birmingham, ,Edgbaston, Birmingham, B15 2TT, UK*
[7]*Hautes Etudes dÍngénieur, 13 rue de Toul, 59000 Lille, France*

SUMMARY

Prostate contours delineation on Magnetic Resonance (MR) images is a challenging and important task in medical imaging with applications of guiding biopsy, surgery and therapy. While a fully automated method is highly desired for this application, it can be a very difficult task due to the structure and surrounding tissues of the prostate gland. Traditional active contours-based delineation algorithms are typically quite successful for piecewise constant images. Nevertheless, when MR images have diffuse edges or multiple similar objects (e.g. bladder close to prostate) within close proximity, such approaches have proven to be unsuccessful. In order to mitigate these problems, we proposed a new framework for bi-stage contours delineation algorithm based on directional active contours (DAC) incorporating prior knowledge of the prostate shape. We first explicitly addressed the prostate contour delineation problem based on fast globally DAC that incorporates both statistical and parametric shape prior model. In doing so, we were able to exploit the global aspects of contour delineation problem by incorporating a user feedback in contours delineation process where it is shown that only a small amount of user input can sometimes resolve ambiguous scenarios raised by DAC. In addition, once the prostate contours have been delineated, a cost functional is designed to incorporate both user feedback interaction and the parametric shape prior model. Using data from publicly available prostate MR datasets, which includes several challenging clinical datasets, we highlighted the effectiveness and the capability of the proposed algorithm. Besides, the algorithm has been compared with several state-of-the-art methods.

KEY WORDS: directional active contours; characteristic function; Bhattacharyya distance; user interaction; parametric shape prior; prostate shape; T_2-weighted MR images; total variational framework

1. INTRODUCTION

Recently, prostate cancer became one of the major health problems in the world, with one in six men affected during their lifetime according to the World Health Organization [1–3]. With many prostate cancers being of low aggressiveness and presenting high risk of radical prostatectomy (impotence, incontinence), accurate risk stratification for each individual cancer is central

*Correspondence to: Foued Derraz, Telecommunications Laboratory/Unité de Traitement de Signaux Biomédicaux, France.
†E-mail: fdrz70@gmail.com

DOI : 10.1002/cnm.2726

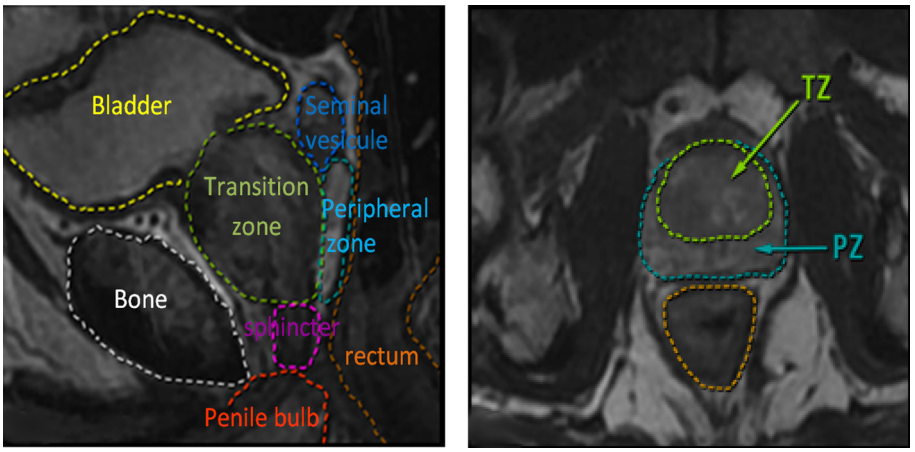

(a) Sagittal prostate MRI slice with organs around the prostate

(b) Axial T_2 prostate MRI slice with manual contour delineated of TZ and PZ

Figure 1. Example T_2-weighted prostate MRI images displaying a central slice. (a) Sagittal and (b) axial T_2-weighted images show manual contours delineation of the TZ (green colour) and PZ (blue colour).

to a successful treatment strategy. Prostate cancer diagnosis is widely based on Prostate Specific Antigen (PSA) levels (e.g. prostate cancer biomarker), testing and trans-rectal ultrasound (TRUS) guided biopsies, which often result in a low sensitivity, and thereby, high rates of re-biopsies [1]. In a clinical practice, overlaying the TRUS guided biopsy image [2] onto the pre-segmented MR image increases the accuracy of prostate biopsy [1, 3, 4] and therefore sought-after is highly desired in a TRUS/Magnetic Resonance Imaging (MRI) guided biopsy system. Pathologists split the prostate gland into four distinct zones [5]: (1) peripheral zone (PZ) ; (2) central zone (CZ); (3) transition zone (TZ); and (4) anterior fibromuscular stroma (Figure 1(a)). The PZ was obtained by subtracting the central gland (CG) including CZ and TZ from the prostate whole gland (Figure 1(b)). During guidance of the biopsy, the prostate is usually considered to have two visible zones on MR images, the CG and the PZ. The CG is assumed to be the outer contour of the prostate minus the PZ [6]. The reason for delineating the contours of these regions is that up to 80% of prostate cancers are located within the PZ [5]. In diagnosing prostate cancer, prostate volume is routinely checked as part of imaging evaluation [7–9], including calculation of volume pre-treatment and post-treatment, biopsy guided intervention [3], radiotherapy planning [1, 6, 10–12], dosimetry [13, 14] and for creating patient-specific anatomical models [15].

In many clinical applications, identifying prostate volume is an attractive option for guiding and monitoring such interventions because of its superior visualization of not only the prostate but also its substructure and surrounding tissues like the bladder and rectum [16, 17]. Other knowledge about the prostate volume, such as shape and anatomic position with respect to surrounding organs, for example, bladder and rectum, is highly desired for treatment planning calculation. The high spatial resolution and soft-tissue contrast offered by MRI makes it the most accurate method available for obtaining this kind of information.

Thus, recent years have seen increased clinical adoption of MRI for treatment planning. An essential role of this technique is to accurately and efficiently delineate the contours of the prostate CG and PZ allowing the detection of small tumors and improvements of cancer staging. In recent years, a wide spread of automated [18–21], semi-automated [9, 13] and interactive [22, 23] prostate contours delineation algorithms have been proposed, a step that has been shown to facilitate efficient MR guided intervention [24–27].

In this context, the correct contours delineation of the prostate is a critical step for any computer aided diagnosis technique because the occurrence and appearance of cancer are dependent on its zonal location [26, 28]. In addition, the ratio of CG volume to whole prostate gland can be a useful metric in many of such clinical applications [26].

Various active contours (AC) segmentation-based algorithms [7] were proposed to delineate prostate contours based on imagery data alone [17, 29, 30]. Using edge-related and region-based features of data images, the aforementioned methods were able of providing reliable contouring results on conditions of moderate noises and unoccluded objects. Unfortunately, such methods are also known to be prone to erroneous delineation in practical scenarios where some parts of the object of interest appear to be occluded, missing or corrupted by strong noises. In these situations, a standard solution is to enhance the contours delineation algorithm through the incorporation of the prior knowledge such as shape or texture. AC model-based algorithms have been widely used for prostate contours delineation in [30–32] and can be split into two classes: those which fully rely on image data [30] and those which incorporate prostate prior shape information [30, 33, 34]. Most of these algorithms consider the contours delineation algorithm as a combination of two competing optimization problems. The first problem maximizes the likelihood of the contour's configuration based on image-dependent data, while the second one minimizes the extent to which the contour violates the shape constraints imposed by the shape prior model.

A variety of algorithms incorporating shape prior models have been proposed in [7, 20, 22, 32, 35, 36] to deal with the complex prostate anatomy and partially missing boundaries, where the prostate shape is approximately assumed to be elliptical. In many cases, this task is a two-part problem. First, one must properly align a set of training shapes such that any variation in shape is not due to alignment. Then, automatic contours delineation based on AC can be performed under the constraint of the learned prostate shapes. However, the alignment of prostate shapes becomes increasingly difficult for a large variation in training shapes or training sets, which renders the aforementioned techniques ineffective. Under such conditions, introducing some prior knowledge about the prostate, such as the general shape, location, intensity and curvature profile of the tissue of interest could help the algorithm to better perform the prostate contours delineation. In addition, tissues surrounding the prostate, such as the bladder, rectum and muscles have overlapping intensity and texture. For some patients, at certain slices, the prostate boundaries may be missing or blended with those surrounding tissues. To overcome this problem, we proposed to combine the shape information of the ellipsoidal prostate region and the directional AC model [22, 37] to boost the accuracy of the prostate contours delineation algorithm. The interaction could constrain the contours delineation algorithm and help it to extract the prostate contours more accurately. For example, the shape prior model in [22, 36, 38] assumes the average shape across a set of manual delineated contours. Subsequently, the AC is constrained to deviate the least from this average shape. A similar approach is exploited in [22, 38] where a different cost function was used to assess the aforementioned deviation. While useful in situations where the shape of the AC needs to be strongly constrained (as it would be the case with occlusions), the performances of methods in [22, 29, 39] strongly degrade when the actual shape of the object happens to deviate considerably from its sample average.

In this paper, we proposed a bi-stage interactive prostate contours delineation algorithm based on fast globally DAC incorporating prior knowledge from MR images. Then, based on globally fast DAC incorporating both shape prior and statistical knowledge, our algorithm is applied to delineate prostate boundary. Next, the result is finely tuned through the user's intervention. Besides, our proposed DAC algorithm can be used in different ways for extracting the contours of TZ boundary and/or CG. By delimiting the contours, the underlying PZ can be identified as well, for further analysis. Our method can be assumed as an interactive contours delineation algorithm guided both by anatomical data and user interaction. In addition, our algorithm can be applied twice to delineate and refine, both PZ contours and TZ contours. The remainder of this paper is organized as follows. In the next section, we describe the basics of our method. In Section 3, the experimental results obtained using our method are illustrated. Conclusions and future work are presented in Section 4.

2. PROSTATE CONTOURS DELINEATION FRAMEWORK

The proposed framework for interactive prostate contours delineation consists of two main steps. In the first step, an automated algorithm is designed to delineate coarsely the shape of prostate. The second step is needed to refine the prostate contour and to correct the misplaced

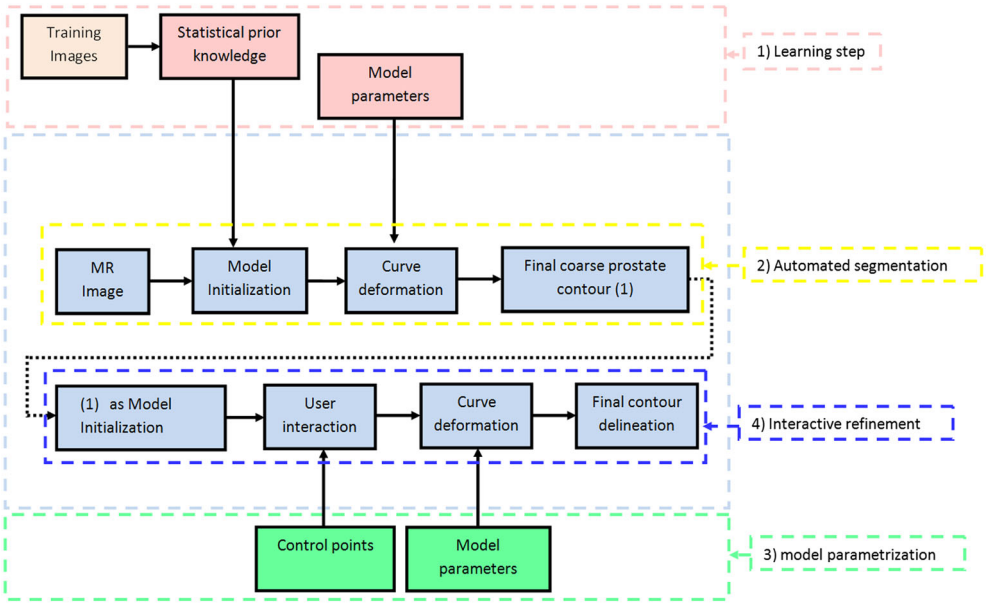

Figure 2. Flowchart of directional active contours-based contours delineation algorithm.

contour curves. As summarized in Figure 2, the proposed algorithm consists of the following steps: the proposed algorithm uses the DAC design for prostate contour delineation: given images and statistical knowledge and shape prior model, the goal is to delineate accurately and efficiently the prostate boundary. More specifically, the statistical knowledge is designed as a convex function of Bhattacharyya distance, which is then incorporated in the formulation of our DAC as data-dependent energy term. While the shape prior knowledge is designed as a parametric shape prior model using a deformable ellipse with pose parameters controlled at each iteration. In the second step, the delineated contours of prostate are refined by adding an interactive user feedback to our DAC algorithm. All these steps are described in detail in the next section.

2.1. Directional active contours in total variation framework

We are interested in a globally interactive contours delineation of prostate using a fast variational algorithm [40–42]. For an image $I : \Omega_I \subset \mathbb{R}^2 \rightarrow \mathbb{R}^+$ defined on an open and bounded domain Ω_I, the fast DAC-based automatic contours delineation consists in extracting one or more contours associated to one or more region domains pertaining to Ω_I. Especially, for a curve placed around an object, DAC-based contours delineation algorithm consists in finding a regular closed curve $\partial\Omega$ by deforming and moving the curve towards the object boundary. Our fast interactive contours delineation algorithm is modeled as the minimization of the following energy criterion [42, 43]:

$$\begin{aligned} E_{DAC}(\chi, \Omega, \psi, \Omega_{ROI}) = & \underbrace{\int_{\partial\Omega} k_D(\mathbf{x}, \mathbf{p})\, da(\mathbf{x})}_{E_b(\partial\Omega)} + \underbrace{\int_{\Omega_I} k_{data}(\mathbf{x}, \Omega)\, \chi(\mathbf{x})\, d\mathbf{x}}_{E_{data}(\chi, I)} \\ & + \lambda_2 \underbrace{\int_{\Omega_I} k_{shape}(\mathbf{x}, \psi)\, \chi(\mathbf{x})\, d\mathbf{x}}_{E_{shape}(\chi, \Omega, \psi)} + \lambda_3 \underbrace{\int_{\Omega_I} k_{user}(\mathbf{x}, \Omega_{ROI})\, \chi(\mathbf{x})\, d\mathbf{x}}_{E_{user}(\Omega, \Omega_{ROI})} \end{aligned} \quad (1)$$

where k_D is the directional boundary descriptor, $da(\mathbf{x})$ is a surface element, λ_2 and λ_3 are the calibration parameters, k_{data} is a data-dependent descriptor that accounts for statistical knowledge, k_{shape} is a shape prior descriptor that matches the boundary to an ellipsoid shape as in [37]

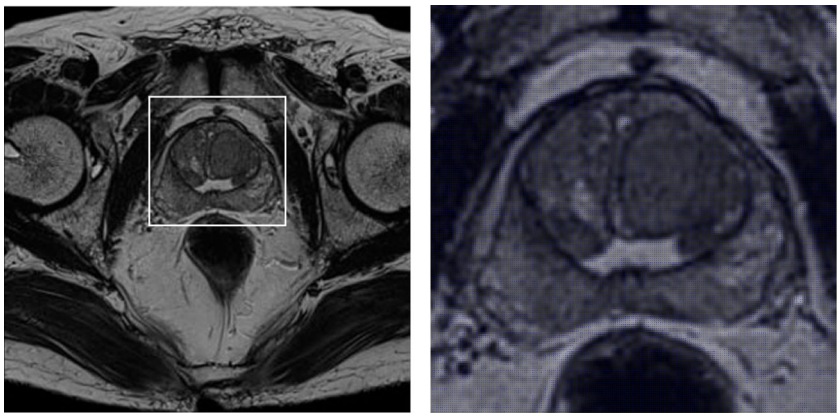

(a) Axial MR slice at the mid-gland prostate and Ω_{ROI} (b) visualization of potential field in Ω_{ROI}

Figure 3. Potential field $[\mathbf{p}_x, \mathbf{p}_y]$. (a) Axial MR slice at the mid-gland prostate and Ω_{ROI} and (b) visualization of potential field in Ω_{ROI}.

and ψ is a vector t of ellipsoid shape parameters. k_{user} delimits the region of interest Ω_{ROI} where the contours could be corrected through user's interaction. The details of these descriptors are reported later in this section . The use of characteristic function or indicator function χ [40] in (1) allows our DAC to be less sensitive to exact values of the parameters (because only thresholding matters with indicator function). Besides, this also enables fast numerical computations involving curves and surfaces without the need to explicitly parameterize these objects. Thus, in the current setting, the subset Ω can be defined using the following indicator function:

$$\chi(\mathbf{x}) = \begin{cases} 1 \ \textit{if} \ \mathbf{x} \in \Omega \\ 0 \ \textit{if} \ \mathbf{x} \notin \Omega_I \backslash \Omega \end{cases} \tag{2}$$

The data-dependent energy term E_{data} is defined as the integral of an extended statistical region descriptor k_{data} using the Bhattacharyya distance [41]. We go through the details of our new descriptor in Section (2.2), k_{shape} is the shape prior descriptor defined as an extended parametric ellipse as defined in [37] to model the prostate shape. The interactive user feedback descriptor k_{user} will be defined in Section (2.4). The data-dependent energy term E_{data} is defined as the integral of the data dependent descriptor k_{data} , detail of which is reported in Section (2.4). To allow our algorithm to delineate contours of the prostate, let an anisotropic boundary descriptor be defined as follows:

$$k_D(\mathbf{x}, \mathbf{p}) = \max_{|\mathbf{p}| \leq 1, \chi} \langle \mathbf{p}, \nabla \chi(\mathbf{x}) \rangle \tag{3}$$

where the potential field, $\mathbf{p}$, is defined as $\mathbf{p} = \left[\mathbf{p}_x, \mathbf{p}_y\right]$ (Figure 3).

The directional descriptor is regarded as scalar product of the potential field $\mathbf{p}$ and $\nabla \chi(\mathbf{x})$. This allows the DAC curves to be attracted by the object boundaries in the maximum direction of gradients and help the curves to rapidly move toward the boundaries of an object in the image. In Equation (3), our descriptor aligns the potential field to the edges founded in an image. This propriety makes the proposed contours delineation algorithm much faster because the topology of the deformed curve is more like the object to be delineated. Our DAC-based contours delineation algorithm can be regarded as bi-stage algorithm. In the first stage, only the anisotropic-dependent descriptor, data-dependent and shape prior model are considered in our contours delineation problem. Our contours delineation problem can be solved by considering $\lambda_3 = 0$. In the second stage, the user feedback is added to our contours delineation problem, $\lambda_3 \neq 0$. In the figure (4), we present a first example of the results of two-stage contours delineation algorithm for only the CG. Inside the CG, the foreground/background statistical priors are introduced by selecting many boxes (green/orange colour). In the first stage, the initialization is considered to be ellipsoid and only

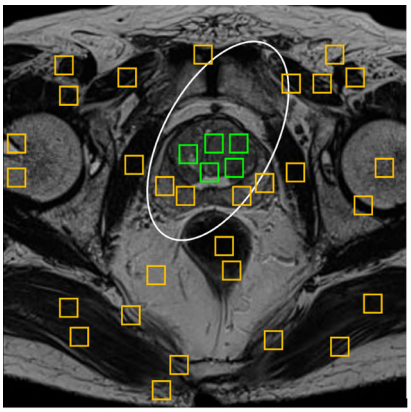

(a) Ellipse curve placed around the prostate mid-gland as initialization of our DAC

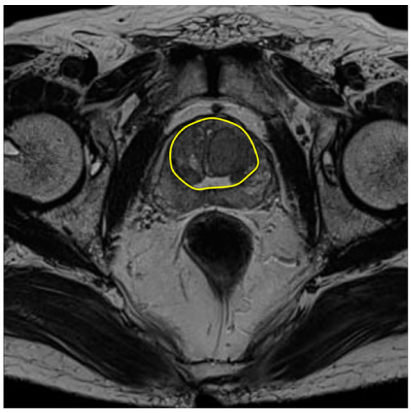

(b) Evolution of DAC after 200 iteration, the DAC incorporates both statistical and parametric shape prior model ($\lambda_1 = 0.8$, $\lambda_2 = 0.9$, $\lambda_3 = 0$)

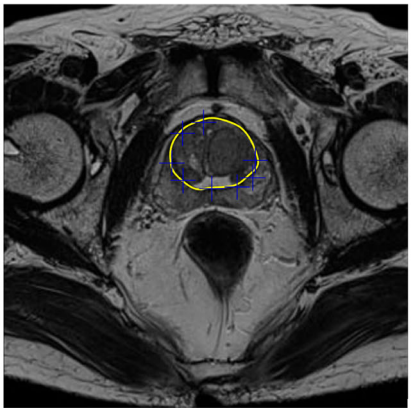

(c) Final Prostate contour delineated using DAC with statistical and parametric shape prior model and without user feedback

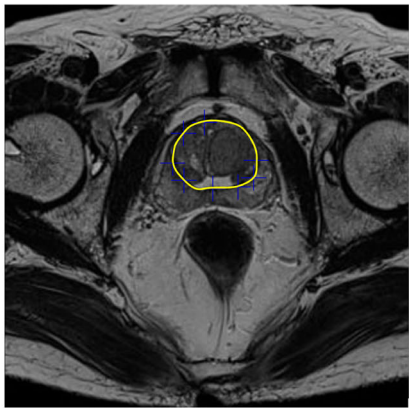

(d) Contour delineated using DAC after user feedback, statistical and parametric shape prior model are also used for ($\lambda_1 = 0.8$, $\lambda_2 = 0.1$, $\lambda_3 = 0.8$)

Figure 4. Example of prostate (central gland (CG) and CG+peripheral zone (PZ)) contours delineation using the directional active contours (DAC) driven by anisotropic boundary descriptor, the DAC incorporates only statistical and shape prior model. (a) Ellipse curve placed around the prostate mid-gland as initialization of our DAC; (b) Evolution of DAC after 200 iteration, the DAC incorporates both statistical and parametric shape prior models ($\lambda_1 = 0.8$, $\lambda_2 = 0.9$, $\lambda_3 = 0$); (c) Final prostate contour delineated using DAC with statistical and parametric shape prior models and without user feedback; and (d) Contour delineated using DAC after user feedback, statistical and parametric shape prior models are also used for ($\lambda_1 = 0.8$, $\lambda_2 = 0.1$, $\lambda_3 = 0.8$).

statistical proprieties of prostate texture are incorporated as learned features without the need of the segmented of the prostate shapes. In the second stage, refined the coarse segmentation done in the first stage by adding user feedback in order to correct and refine the segmentation. The parameter tunes used in the first coarse stage differ from those used in the second stage. In a second example (Figure 5), our algorithm learned both statistical priors of the CG and PZ (foreground/background). The solution nature of contours delineation problem in (1) was already demonstrated in [42] by rewriting the directional boundary descriptor in TV framework using indicator function [40] and extended to general Wulff shape families [22]. The dual energy scheme of the DAC in (1) is given by the following:

$$E_{DAC}(\mathbf{p}) = \int_{\Omega_I} \min\left(0, div(\mathbf{p}) + k_{data}(\mathbf{x}, \Omega) + \lambda_2 k_{shape}(\mathbf{x}, \psi) + \lambda_3 k_{user}(\mathbf{x}, \Omega_{ROI})\right) d\mathbf{x} \quad (4)$$

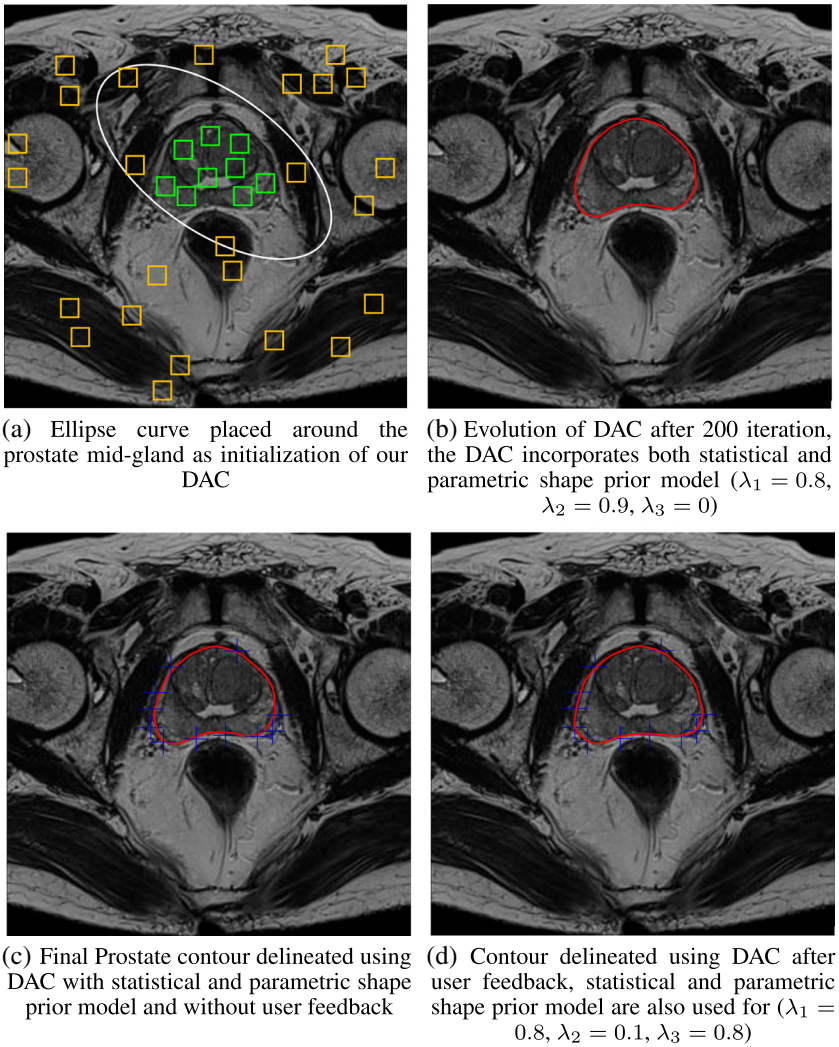

(a) Ellipse curve placed around the prostate mid-gland as initialization of our DAC

(b) Evolution of DAC after 200 iteration, the DAC incorporates both statistical and parametric shape prior model ($\lambda_1 = 0.8$, $\lambda_2 = 0.9$, $\lambda_3 = 0$)

(c) Final Prostate contour delineated using DAC with statistical and parametric shape prior model and without user feedback

(d) Contour delineated using DAC after user feedback, statistical and parametric shape prior model are also used for ($\lambda_1 = 0.8$, $\lambda_2 = 0.1$, $\lambda_3 = 0.8$)

Figure 5. Example of prostate (central gland (CG)and CG+peripheral zone (PZ)) contours delineation using the directional active contours (DAC) driven by anisotropic boundary descriptor, the DAC incorporates only statistical and shape prior model. (a) Ellipse curve placed around the prostate mid-gland as initialization of our DAC; (b) Evolution of DAC after 200 iteration, the DAC incorporates both statistical and parametric shape prior model ($\lambda_1 = 0.8$, $\lambda_2 = 0.9$, $\lambda_3 = 0$); (c) Final prostate contour delineated using DAC with statistical and parametric shape prior model and without user feedback; and (d) Contour delineated using DAC after user feedback, statistical and parametric shape prior model are also used for ($\lambda_1 = 0.8$, $\lambda_2 = 0.1$, $\lambda_3 = 0.8$).

which is maximized with respect to the potential field $\mathbf{p}$ subject to $|\mathbf{p}| \leq 1$, thus the primal energy of DAC in (1) and dual energy functional (4) can be formulated in a primal-dual setting as follows:

$$E_{DAC}(\chi, \psi, \Omega_{ROI}, \mathbf{p}) = \int_{\Omega_I} \max_{|\mathbf{p}| \leq 1} \underbrace{(\langle \mathbf{p}, \nabla \chi(\mathbf{x}) \rangle)}_{k_D(\mathbf{x},\mathbf{p})} da(\mathbf{x}) + \int_{\Omega_I} k_{data}(\mathbf{x}, \Omega)\, \chi(\mathbf{x})\, d\mathbf{x} + \lambda_2 \int_{\Omega_I} k_{shape}(\mathbf{x}, \psi)\, \chi(\mathbf{x})\, d\mathbf{x} + \lambda_3 \int_{\Omega_I} k_{user}(\mathbf{x}, \Omega_{ROI})\, \chi(\mathbf{x})\, d\mathbf{x} \tag{5}$$

and the respective gradient descent (for χ) and ascent (for the potential field $\mathbf{p}$) corresponding are as follows:

$$\begin{cases} \chi(\mathbf{x}, \tau = 0) = \chi_0 = \mathbf{1}_{\min(dist(\mathbf{x}, \partial\Omega_0))} \\ \frac{\partial \mathbf{p}}{\partial \tau} = -\nabla \chi(\mathbf{x}, \tau) \\ \frac{\partial \chi(\mathbf{x}, \tau)}{\partial \tau} = div(\mathbf{p}) - k_{data}(\mathbf{x}, \Omega) - \lambda_2 k_{shape}(\mathbf{x}, \psi) - \lambda_3 k_{user}(\mathbf{x}, \Omega_{ROI}) \end{cases} \tag{6}$$

where τ is an artificial time parameter chosen with the respect to the Courant–Friedrichs–Lewy (CFL) condition [44], χ_0 is the initialized characteristic function corresponding to the initial binary region $\mathbf{1}_{\min(dist(\mathbf{x}, \partial\Omega_0))}$. This binary region also correspond to the initial contour curve $\partial\Omega_0$. In the next section, we introduced extended Bhattacharyya distance-based region descriptor as an additive energy term in the formulation of our DAC.

2.2. Data-dependent energy term

In this section, we introduced a convex data-dependent energy term that uses Bhattacharyya distance as opposed to existing models using Chernoff distance, Kullback–Leibler distance and Cauchy–Schwarz distance [45]. Bhattacharyya distance was originally introduced in [46], in the formulation of data-dependent energy term, as positive, symmetric and it goes to infinity when the overlap between the two Probability Densities Functions (PDF) goes to zero. Statistical prior knowledge are incorporated in the formulation of our DAC as an additive energy term of the region descriptor. Expressing surface of delineated contours in terms of its associated statistical region descriptor in term of characteristic function χ leads to define our region descriptor as convex function of the Bhattacharyya distance [45, 46], which now becomes a function of χ:

$$E_{data}(\chi, I) = \lambda_1 \int_{\Omega_I} \sqrt{p(I, \Omega)\, p(\mathbf{x}_f)}\, d\mathbf{x} + (1 - \lambda_1) \int_{\Omega_I} \sqrt{p(\mathbf{x}_b)\, p(I, \Omega_I \backslash \Omega)}\, d\mathbf{x} \tag{7}$$

where λ_1 is calibration factor parameter, $\mathbf{x}_f$, the learned pixels of prostate tissues and $\mathbf{x}_b$ are the learned pixels prostate surrounding tissues. Because the shape of the rectum in the case of guided intervention can be very close to a deformable ellipse. In the absence of statistical knowledge of prostate and surrounding tissues, the DAC can delineate the contours of the rectum instead of the prostate. To avoid this difficulty, we learned our region descriptor respectively statistics of prostate tissues $\mathbf{x}_f$, and the background tissues $\mathbf{x}_b$. The region descriptor learned prostate tissues (CG and/or PZ) by selecting many boxes inside the prostate and others are selected outside the prostate. We construct two dictionaries for the two tissues using principal component analysis. Each term of data-dependent energy minimized respectively the Bhattacharyya distance between $\mathbf{x}_f$ and $\mathbf{x}_b$. Tissues in the image are modeled using non-parametric (PDF) $p(I, \Omega)$, which can be calculated according to the Parzen kernel [47] (Figure 6(b) and (d):

$$p(I, \Omega) = \frac{1}{|\Omega|} \int_{\Omega_I} G_{\sigma_{ker}}(I - I(\Omega))\, d\mathbf{x} \tag{8}$$

where $G_{\sigma_{ker}}$ denotes the Gaussian kernel, σ_{ker} the variance and $|\Omega|$ the surface of delineated region. σ_{ker} could be selected empirically in the range of 0.5 to 0.8.

The performances of our Bhattacharyya-based convex distances compared with traditional Bhattacharyya, Chernoff-based distance and Kullback-Leibler divergence. The reason is that both Kullback–Leibler and Chernoff are ratio measures and become unstable because of sampling errors. In the case of Kullback–Leibler distance, when only few samples are available because of the limited number of gray-levels in the image, the pdfs estimated p_{in} and p_{out} in the case of Kullback–Leibler will be sparse and the ratio $\log_{p(\mathbf{x}_f) \to 0} \left(\frac{p(I, \Omega_I)}{p(\mathbf{x}_f)} \right) \to -\infty$ or $\log_{p(I, \Omega_I) \to 0} \left(\frac{p(\mathbf{x}_f)}{p(I, \Omega_I)} \right) \to \infty$ causing numerical instability in the evaluation of the Kullback–Leibler divergence [45]. This problem does not occur in our convex Bhattacharyya distance, which is a balanced measure.

Subsequently, optimal delineated contours can be supplanted by an equivalent problem of finding an optimal characteristic function as given in (1). Because of the absence of a closed form solution

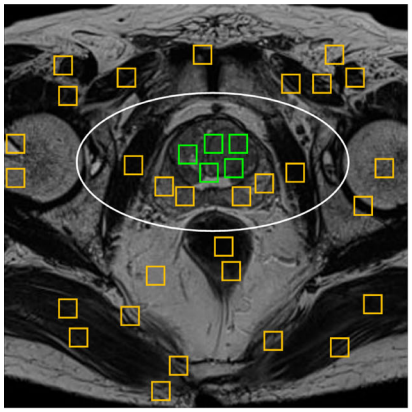

(a) Final Prostate contour delineated using DAC with statistical and parametric shape prior model and without user feedback

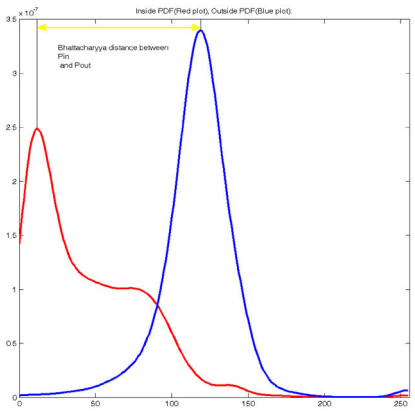

(b) statistical prior model are also used for ($\lambda_1 = 0.8$),the PDF calculated inside the CG (blue color), the PDF outside the prostate in red color

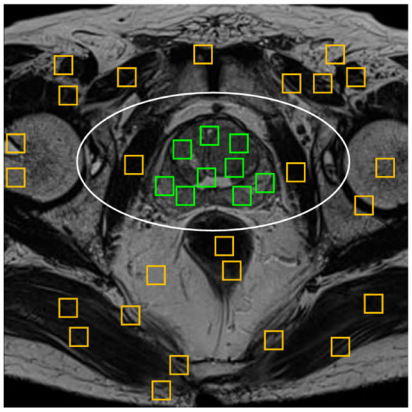

(c) Final Prostate contour delineated using DAC with statistical and parametric shape prior model and without user feedback

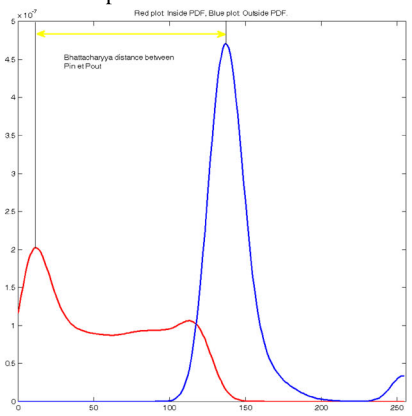

(d) statistical prior model are also used for ($\lambda_1 = 0.8$),the PDF calculated inside the CG (blue color), the PDF outside the prostate in red color

Figure 6. Minimization process of Bhattacharyya distance between probability densities function (PDF) inside/outside the prostate (central gland (CG) and CG+peripheral zone (PZ)). (a) Final prostate contour delineated using directional active contours (DAC) with statistical and parametric shape prior model and without user feedback; (b) statistical prior model are also used for ($\lambda_1 = 0.8$), the PDF calculated inside the CG (blue colour) and the PDF outside the prostate in red colour; (c) Final prostate contour delineated using DAC with statistical and parametric shape prior model and without user feedback; and (d) Statistical prior models are also used for ($\lambda_1 = 0.8$), the PDF calculated inside the CG (blue colour)and the PDF outside the prostate in red colour.

to our contours delineation problem, a numerical scheme for solving our contours delineation problem in (5) is needed. In our case, the problem in (7) is solved by the means of a steepest descent procedure, which prescribes the approximation as a stationary point of the sequence of solutions produced by the gradient shape [42] as given by the following:

$$\left\langle \frac{\partial E_{data}\left(\chi\left(\tau\right),I\right)}{\partial \tau}, \xi \right\rangle = \int_{\partial\Omega} k_{data}\left(\mathbf{x},\chi\right)\left\langle \xi, N_{\partial\Omega}\right\rangle da\left(\mathbf{x}\right) \tag{9}$$

where $N_{\partial\Omega}$ is normal vector to the evolving DAC curve, ξ is an artificial vector ensuring the alignment to $N_{\partial\Omega}$ and τ is an artificial time parameter. When ξ is aligned to $N_{\partial\Omega}$, the velocity corresponding to the data-dependent energy term

$$k_{data}(\mathbf{x},\Omega)=\frac{1}{2}\left(\begin{array}{c}\frac{\lambda_1}{|\Omega|}\sqrt{p\left(\mathbf{x}_f\right)p\left(I,\Omega\right)}-\frac{1-\lambda_1}{|\Omega_I\backslash\Omega|}\sqrt{p\left(\mathbf{x}_b\right)p\left(I,\Omega_I\backslash\Omega\right)}+\\ \frac{1-\lambda_1}{|\Omega_I\backslash\Omega|}\int\limits_{\Omega_I}\sqrt{\frac{p(\mathbf{x}_b)}{p(I,\Omega_I\backslash\Omega)}}\left(G_{\sigma_{\ker}}\left(I-I\left(\Omega\right)\right)-\sqrt{p\left(I,\Omega_I\backslash\Omega\right)}\right)dI-\\ \frac{\lambda_1}{|\Omega|}\int\limits_{\Omega_I}\sqrt{\frac{p(\mathbf{x}_f)}{p(I,\Omega)}}\left(G_{\sigma_{\ker}}\left(I-I\left(\Omega\right)\right)-\sqrt{p\left(I,\Omega\right)}\right)dI\end{array}\right) \tag{10}$$

where τ is an artificial time parameter, introduced to allow the characteristic function to evolve into a family $\chi(\mathbf{x},t)$.

2.3. Parametric shape prior model

The incorporation of deformable ellipse as parametric shape prior model in the formulation of our DAC is a relatively attractive approach for prostate contours delineation algorithm as most prostates conform well to these representations as suggested by other studies [20, 37, 48]. To obtain the prostate shape information, we use a two-step procedure where a rough ellipsoid is assigned initially, which is then refined in the next stage. More specifically, because the prostate shapes are not ideal ellipsoids, we use the parametric ellipse to fit the prostate more accurately. In the first step, the prostate contours are roughly fitted by a deformable ellipse as follows:

$$F(\mathbf{x},\psi)=1-\left(\frac{(x-a)\cos(\theta)-(y-b)\sin(\theta)}{r_1}\right)^2+\left(\frac{(y-b)\cos(\theta)-(x-a)\sin(\theta)}{r_2}\right)^2 \tag{11}$$

The shape parameters $\psi=(a,b,r_1,r_2,\theta)$ define an ellipsoid, where (a,b) is the center of the ellipsoid, (r_1,r_2) the lengths of the semi axes and θ the orientation of the ellipsoid $F(\mathbf{x},\psi)$. To obtain an ellipsoid $F(\mathbf{x},\psi)$, which best fits the prostate shape, we borrow the idea of least-square minimization and super quadric foreground–background function presented in [37]. Based on the implicit representation of the parametric ellipsoid, we define the function called the inside/outside characteristic function framework:

$$\chi_{shape}(\mathbf{x},\psi)=\begin{cases}1 & if\ \ F(\mathbf{x},\psi)<=0\\ 0 & if\ \ F(\mathbf{x},\psi)>0\end{cases} \tag{12}$$

To find the best fitting parameters ψ, of $F(\cdot)$ with a minimum corresponding to the ellipsoid that best fits the given prostate shape, we define a shape fitting function as distance between evolving shape and the best fitted ellipsoid:

$$=\underset{(a,b,r_1,r_2,\theta)}{\arg\min}\left\{E_{shape}(\chi,\Omega,\psi)\right\}=\underset{(a,b,r_1,r_2,\theta)}{\arg\min}\left\{\int\limits_{\Omega}\left|\chi_{shape}(\mathbf{x},\psi)-\chi(\mathbf{x})\right|^2d\mathbf{x}\right\} \tag{13}$$

For the pixels inside of the deformable ellipse, we have $\chi(\mathbf{x})=1$ and for pixels outside of the deformable ellipse, we have $\chi(\mathbf{x})=0$. If the contours of the prostate are perfectly delineated, $\chi(\mathbf{x})$ is the ideal prostate mask, the deformable ellipse converges to the smallest deformable ellipse, which best fits the prostate shape. In practice, we simplify the estimation of the deformable ellipse. To do so, the cost function in Equation (13) is minimized by iterative gradient descent method with respect to the unknown shape parameters ($\psi_1=a$, $\psi_2=b$, $\psi_3=r_1$, $\psi_4=r_2$, $_5=\theta$) is as follows:

$$\frac{\partial\psi_i}{\partial t}=\int\limits_{\Omega}\left|\chi_{shape}(\mathbf{x},\psi)-\chi(\mathbf{x})\right|F_{\psi_i}\left(\mathbf{x}^*,\ \ \right)\delta\left(F\left(\mathbf{x}^*,\ \ \right)\right)d\mathbf{x},i=1,...,5 \tag{14}$$

where $F_{\psi_i}=\frac{\partial F}{\partial\psi_i}$ and $\mathbf{x}^*$ is defined as function aligned pixel $\mathbf{x}$ and $\delta(\cdot)$ is the Dirac function.

By observing the deformable ellipse fitting results as shown in Figure (7) that our model is able to roughly handle the prostate shape as shown in Figure 7(b) and (d). To further improve the shape result, we apply model the shape using the best fitting parameters ψ more accurately. The shape

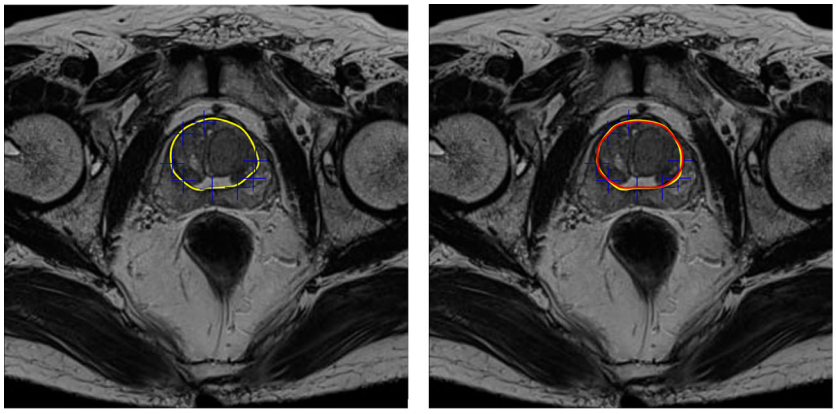

(a) Final Prostate contour delineated using DAC with statistical and parametric shape prior model and without user feedback

(b) Contour delineated using DAC after user feedback, statistical and parametric shape prior model are also used for ($\lambda_1 = 0.8$, $\lambda_2 = 0.1$, $\lambda_3 = 0.8$),in yellow color, the final delineated contour and in red color the ground truth, control points by the user in blue color

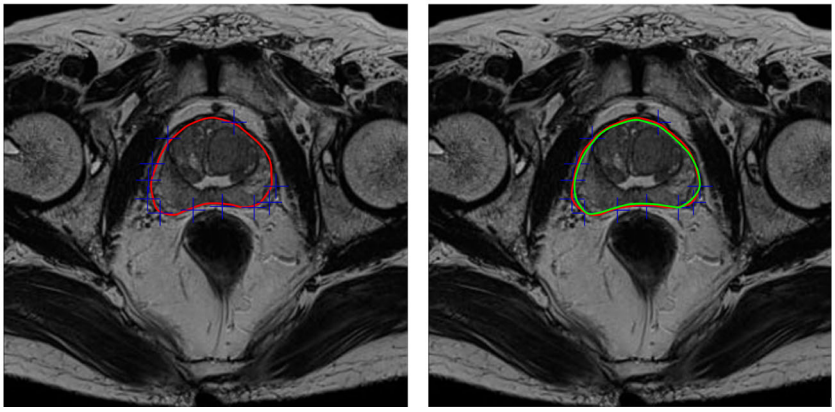

(c) Final Prostate contour delineated using DAC with statistical and parametric shape prior model and without user feedback

(d) Contour delineated using DAC after user feedback, statistical and parametric shape prior model are also used for ($\lambda_1 = 0.8$, $\lambda_2 = 0.1$, $\lambda_3 = 0.8$),in red color, the final delineated contour and in green color the ground truth, control points by the user in blue color

Figure 7. Example of prostate (central gland (CG) and CG+peripheral zone (PZ)) contours delineation using the directional active contours (DAC) driven by anisotropic boundary descriptor, the DAC incorporates only statistical and shape prior model. (a) Final Prostate contour delineated using DAC with statistical and parametric shape prior model and without user feedback; (b) Contour delineated using DAC after user feedback, statistical and parametric shape prior model are also used for ($\lambda_1 = 0.8$, $\lambda_2 = 0.1$, $\lambda_3 = 0.8$) in yellow colour, the final delineated contour and in red colour the ground truth, control points by the user in blue colour; (c) Final prostate contour delineated using DAC with statistical and parametric shape prior model and without user feedback; and (d) Contour delineated using DAC after user feedback, statistical and parametric shape prior model are also used for ($\lambda_1 = 0.8$, $\lambda_2 = 0.1$, $\lambda_3 = 0.8$) , in red colour, the final delineated contour and in green colour the ground truth, control points by the user in blue colour.

information is updated by finding an ellipse that best fits each MR image and defining the parametric shape prior model based DAC model. When the statistical region descriptor is highly weighted (high value of the calibration factor λ_1, delineated contours provided by our DAC are close to those delineated by the clinical expert and the shape is less than an ellipse. However, when the parametric shape prior model is highly weighted (less value of λ_1 and high value of λ_2), the shape of delineated contours are close to an ellipse, and less close to those done by the expert. In two cases, the automatic

delineation process gives unsatisfactory results. To obtain a prostate shape with respect of the two terms, we consider that the weight of the region descriptor and parametric shape prior model are balanced. The delineation process is completed by user interaction in the second step by choosing a high value of λ_3. In Equation (1), the second term incorporates the statistical knowledge, this helps our algorithm to the textured region of the prostate. Many regions in the image can have the same texture. The third term helps our contours delineation algorithm to locate only the texture region with a shape near an ellipse. If the second term is omitted, our model delineates any object of an ellipsoid shape and the rectum contour can be delineated instead of the prostate shape.

2.4. Interactive user feedback

User interaction plays an important role in the contour delineation of medical images, where a user intervention is often suggested as an additional source of information. This technique leverages the expert knowledge to produce accurate delineation of anatomical structures, which facilitates measurement and diagnosis of various diseases. In this paper, we formulate the user interaction as an additive energy term of our DAC model where the user selects a region of interest Ω_{ROI} through some candidate points that will be employed to refine the segmentation result accordingly. Let $(\{\mathbf{x}_i\}_{i=1}^n$ denote the set of n user feedback points. The user feedback $L : \Omega_{ROI} \rightarrow \mathbb{R}$ is defined as follows:

$$L(\mathbf{y}) = \chi(\mathbf{y}) + \frac{1}{n}\{1 - \chi(\mathbf{y})\} \sum_{i=1}^{n} \int_{\mathbf{z}\in\Omega_{ROI}} \delta(\mathbf{z} - \mathbf{x}_i)\, d\mathbf{z} \tag{15}$$

where $\delta(\mathbf{z})$ is the Dirac delta function and Ω_{ROI} is local region. Hence, for each pixel in the local region $\left(\mathbf{y} \in \{\mathbf{y}_i\}_{i=1}^n\right)$:

$$L(\mathbf{y}) = \begin{cases} 0 & \mathbf{y} \in \Omega_{\mathbf{x}} \\ 1 & \mathbf{y} \in \Omega \backslash \Omega_{\mathbf{x}} \\ \chi(\mathbf{y}) & \textit{not marked} \end{cases} \tag{16}$$

where $\Omega_{\mathbf{x}}$ is the local region where the pixels to be corrected could be selected. If $L(\mathbf{x}) = 0$, the feedback points are situated inside the prostate region delineated in first step by our automated algorithm and $L(\mathbf{x}) = 1$ if a feedback point is situated outside the prostate region. Finally, if a pixel is not marked, then the indicator function is identical to $(L(\mathbf{x}) = \chi(\mathbf{x}))$ (Figure 8(b)). The indicator function $L(\mathbf{x})$ is used in the formulation of the user feedback energy term that incorporates the interaction user:

$$E_{user}(\Omega, \Omega_{ROI}) = \int_{\mathbf{x}\in\Omega} \int_{\mathbf{y}\in\Omega_{ROI}} |L(\mathbf{y}) - \chi(\mathbf{x})|^2 e^{-\frac{|\mathbf{x}-\mathbf{y}|^2}{2\sigma^2}}\, d\mathbf{x} d\mathbf{y} \tag{17}$$

The algorithm supports two modes of user feedback. The user may either draw a cross such that its eccentricity and orientation determine the entries of the variance coefficient σ or can provide a point-wise mouse click. In this work, only the second mode is considered for its simplicity. The interactive energy functional E_{user} is minimized, w.r.t the evolving domain $\Omega(\tau)$, is done with the shape derivative tool [40, 42, 49]. Thus, the Eulerian derivative of E_{user} in the normal direction is as follows:

$$\left\langle \frac{\partial E_{user}(I, \Omega(\tau))}{\partial \tau}, \xi \right\rangle = \int_{\partial\Omega} k_{user}(\mathbf{x}, \Omega_{ROI}) \langle \xi, N_{\partial\Omega} \rangle\, da(\mathbf{x}) \tag{18}$$

where the user interaction velocity is expressed as follows:

$$k_{user}(\mathbf{x}, \Omega_{ROI}) = \int_{\mathbf{y}\in\Omega_{ROI}} |L(\mathbf{y}) - \chi(\mathbf{x})|^2 e^{-\frac{|\mathbf{x}-\mathbf{y}|^2}{2\sigma^2}}\, d\mathbf{y} \tag{19}$$

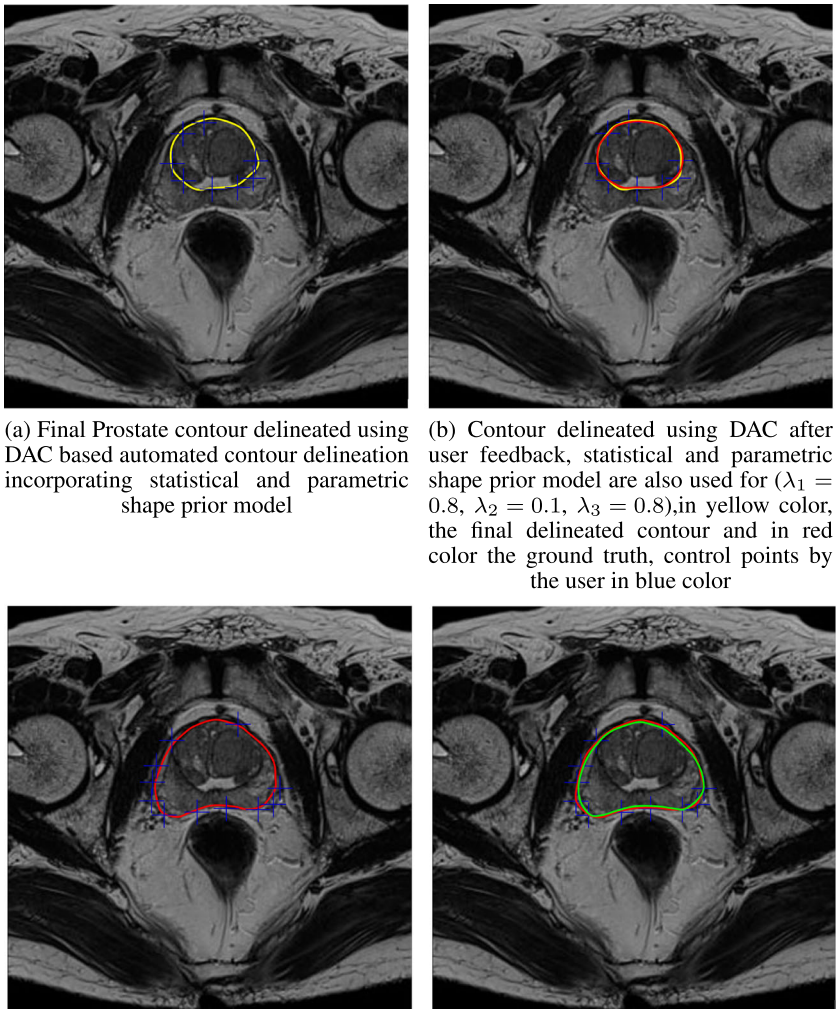

(a) Final Prostate contour delineated using DAC based automated contour delineation incorporating statistical and parametric shape prior model

(b) Contour delineated using DAC after user feedback, statistical and parametric shape prior model are also used for ($\lambda_1 = 0.8$, $\lambda_2 = 0.1$, $\lambda_3 = 0.8$),in yellow color, the final delineated contour and in red color the ground truth, control points by the user in blue color

(c) Final Prostate contour delineated using DAC based automated contour delineation incorporating statistical and parametric shape prior model,control points by the user in blue color

(d) Contour delineated using DAC after user feedback, statistical and parametric shape prior model are also used for ($\lambda_1 = 0.8$, $\lambda_2 = 0.1$, $\lambda_3 = 0.8$),in red color, the final delineated contour and in green color the ground truth, control points by the user in blue color

Figure 8. Prostate contour refinement (central gland (CG) and CG+peripheral zone (PZ)) contour delineation using the directional active contours (DAC) driven by anisotropic boundary descriptor, the DAC incorporates only statistical and shape prior model. (a) Final prostate contour delineated using DAC-based automated contour delineation incorporating statistical and parametric shape prior model; (b) Contour delineated using DAC after user feedback, statistical and parametric shape prior model are also used for ($\lambda_1 = 0.8, \lambda_2 = 0.1, \lambda_3 = 0.8$), in yellow colour, the final delineated contour and in red colour the ground truth, control points by the user in blue colour; (c) Final prostate contour delineated using DAC-based automated contour delineation incorporating statistical and parametric shape prior model,control points by the user in blue colour; and (d) Contour delineated using DAC after user feedback, statistical and parametric shape prior model are also used for ($\lambda_1 = 0.8, \lambda_2 = 0.1, \lambda_3 = 0.8$), in red colour, the final delineated contour and in green colour the ground truth, control points by the user in blue colour.

In Figure 8(b) and (c), we illustrate our contours delineation process. Our second steep interactive contours delineation algorithm is initialized with contours issued from the first steep automated contours delineation based on DAC using both statistical and parametric shape prior model. This curve in white colour is superposed the ground truth in red colour (Figure 8(a). The user could selects points with a mouse click around the automated delineated contours of the prostate. The

interactive delineation process is launched using our DAC-based algorithm and the additive user feedback term. At each iteration, our algorithm uses the statistical and shape prior model to readjust the contours position on the true boundaries of the prostate. When the user believes that the contours shape is close to the true shape of the prostate, then the delineation process can be canceled. The algorithm doing such task can be summarized as follows:

Algorithm 1 Coarse prostate contour delineation using DAC algorithm

Require: ε, μ, σ
  $\lambda_1 \leftarrow$ *tunning parameter*
  $\lambda_2 \quad 0$
  initial parameter
  $\mathbf{p}^0$ *initial potential field*
  while $\left|\chi^{k+1} - \chi^k\right| \geqslant \varepsilon$ **do**
    $\mathbf{p}^{k+1} \quad \tau \cdot \mathbf{p}^k - \tau \cdot \nabla\chi\left(\mathbf{x}, \tau\right)$
    $\chi^{k+1} \quad \chi^k + div\left(\mathbf{p}^k\right) - k_{data}\left(\mathbf{x}, \Omega\right) - \lambda_2 k_{shape}\left(\mathbf{x}, \psi\right)$
  end while
  $\chi^*\left(\mathbf{x}\right) \quad \chi^{k+1}\left(\mathbf{x}\right)$

Algorithm 2 Second stage: refine prostate shape using user feedback in DAC algorithm

Require: ε, μ, σ
  $\lambda_1 \leftarrow$ *user input*
  $\lambda_2 \leftarrow$ *user input*
  $\lambda_3 \leftarrow$ *user input*
  from coarse segmentation
  $\mathbf{p}^0$ *from coarse segmentation*
  χ^0 *from coarse segmentation*
  while $\left|\chi^{k+1} - \chi^k\right| \geqslant \varepsilon$ **do**
    $\mathbf{p}^{k+1} \quad \tau \cdot \mathbf{p}^k - \tau \cdot \nabla\chi\left(\mathbf{x}, \tau\right)$
    $\chi^{k+1} \quad \chi^k + div\left(\mathbf{p}^k\right) - k_{data}\left(\mathbf{x}, \Omega\right) - \lambda_2 k_{shape}\left(\mathbf{x}, \psi\right) - \lambda_3 k_{user}\left(\mathbf{x}, \Omega_{ROI}\right)$
  end while
  $\chi^*\left(\mathbf{x}\right) \quad \chi^{k+1}\left(\mathbf{x}\right)$

3. RESULTS

3.1. Data

Two types of datasets were employed in our study. The first, MR datasets, contain 50 patients acquired using a 1.5T Philips Gyroscan (Philips Medical Systems) at the Saint Philibert Hospital, Lille, France. Each patient has one axial scan. The MR protocol is such that Turbo Spin-Echo (TSE) ($T_2 - w$) and acquisition (TR $=$ 8868.72 ms or 4434.36 ms, TE $=$ 120 ms, angle $=$ 90, FOV $=$ 100 mm) with 3-mm axial slice thickness. The size of each image is 512×512 and the pixel resolution is 0.3 mm $\times$ 0.3 mm. Because TSE maps provide better anatomical shape and contrast between the prostate gland and other tissue, we apply our method to $T_2 - w$ image datasets. The second dataset is acquired from the public MICCAI Grand Challenge 2012 datasets, which is the largest dataset publicly available, which allows us to compare our method to the state of art methods reported in MICCIA challenge workshop [24]. We will refer the MICCAI Grand Challenge 2012 on the Prostate MR Image Segmentation by PROMISE12 (available at: http://promise12.grand-challenge.org/Results).

The PROMISE12 [24] aims at evaluating and comparing algorithms in an independent and standardized way for the task of Prostate contours delineation. The organizers made publicly available two datasets through their website. A dataset of labeled MR images, which can be used to

train the contour delineation algorithm, and an unlabeled dataset on which the algorithm should be tested. The website also allows us to quantitatively evaluate the contours delineation results on the unlabelled dataset using the associated ground truth database and to publish the resulting scores. This project is an original initiative to provide an unbiased comparison between prostate contours delineation.

3.2. Prostate contours delineation process

The contours delineation algorithm is initialized by closed ellipse shape, which is used to approximate the CG. The smooth closed surface approximates the prostate shape and provides a reasonably good initialization condition. The initial PDFs for inside and outside regions of the prostate (CG + PZ), are calculated based on the user-initialized surfaces, respectively. Our contours delineation algorithm is initialized by an arbitrary contour. In the first step, prostate contours will be delineated coarsely in 55 seconds/slice. In the second step, after the control points will be selected, and a refinement is processed also fixed by the user are not uniformly distributed. Trivially, higher Since the number of control points, better is increased the delineated contour of prostate is better. In the second step, the algorithm takes 40 s and for the whole prostate gland, the contours delineation process takes 3 min.

3.3. Evaluation metrics

For all datasets used in this study, the prostate was manually outlined by a clinical expert, which is provided as the ground truth. Given that the number of the slices is generally small, the leave-one out method is employed to show interactive contours delineation results on 50 datasets (mid gland, base and apex). To determine the apex and base, the prostate was divided into three approximately equal parts in the slice dimension (the caudal 1/3 of the prostate volume was considered apex, the cranial 1/3 was considered base). To compare the performance of the proposed algorithm with that of other methods, our statistical contours delineation results were used. The metrics used in this study are widely used for the evaluation of contours delineation algorithms in related studies; namely, the overlap between manual delineated volume and automated delineation is evaluated using the Dice Similarity Coefficient (DSC) [50, 51]:

$$DSC\,(A, B) = 2\frac{|S\,(A) \bigcap S\,(B)|}{|S\,(A)| + |S\,(B)|} \tag{20}$$

where $|S\,(A)|$ is the surface delineated by the reference contours and $|S\,(B)|$ is the surface delineated by our algorithm.

To evaluate the accuracy of the proposed algorithm, the manual delineated contours are often considered as the gold standard. Generally, the similarity or the distance between the automatic and the manual delineated contours is used to compare the accuracy of different algorithms. Most evaluation measures are based on shape distance and area overlap. The Absolute Relative Volume Difference is one of the most valuable tool used in our study and can be calculated as follows:

$$RVD\,(A, B) = 100 \times \left|\frac{|S\,(A)|}{|S\,(B)|} - 1\right| sign\left(\frac{|S\,(A)|}{|S\,(B)|} - 1\right) \tag{21}$$

Other coefficients like the percentage of the absolute difference between the volumes (RVD) [51], the average boundary distance (ABD), the average over the shortest distances between the boundary points of the volumes [51] and the 95% Hausdorff distance (95%HD) [16] can also be used. Note that although we use the RVD to measure algorithm performance (both under-optimization and over-optimization are equally bad), the RVD results were also presented, which makes it possible to identify if algorithms on average tend to over-delineate or under-delineate the prostate contour. For both the 95th percentile HD and the average boundary distance, we first extract the surfaces of the manual delineated contour and the contour delineated by our algorithm. The regular HD is then defined as follows:

$$HD\left(A,B\right)=\max_{a\in S_a(A)}\left(\min_{b\in S_b(B)}\left(d\left(a,b\right)\right)\right) \tag{22}$$

where $S_b\left(B\right)$ and $S_b\left(B\right)$ are the sets of surface points of the reference and delineated surface d is the Euclidean distance. As the normal Hausdorff distance is very sensitive to outliers, we use the 95th percentile of the asymmetric Hausdorff distances instead of the maximum. Finally, the ABD is defined as follows:

$$ABD\left(S_a\left(A\right),S_b\left(B\right)\right)=\frac{1}{N_a+N_b}\left(\sum_{a\in X_s}\min_{a\in S_a(A)}\left(d\left(a,b\right)\right)+\sum_{b\in S_b(B)}\min_{a\in S_a(A)}\left(d\left(a,b\right)\right)\right) \tag{23}$$

All validation metrics were calculated for the entire prostate gland, CG and PZ in the three respective regions. In addition, the coefficient-of-variation (CV) [52] of DSC was used to evaluate the intra-observer and inter-observer variability of our method. We chose both boundary and volume metrics to give a more complete view of accuracy, that is, in radiotherapy boundary-based metrics would be more important, whereas in volumetry, the volume metrics would be more important. In addition, the evaluation of these metrics over the entire prostate volume, we also calculated them specifically for the apex and base parts of the prostate, because these parts are very important to delineate correctly, for example in radiotherapy and TRUS/MR fusion. Moreover, these are the most difficult parts to delineate because of the large inter-patient variability and differences in slice thickness.

3.4. Comparison with other prostate contours delineation methods

In this study, we describe and evaluate a new global optimization-based DAC algorithm to delineate the prostate contours from MR datasets in a numerically stable and efficient way. The experimental results for public dataset (PROMISE'12) and our dataset show that our algorithm is able of providing accurate, robust and efficient algorithm in terms of high accuracy and efficiency while achieving low intra-observer and inter-observer variability introduced by user feedback.

We compare our method to state-of-the-art prostate contour delineation such as the modified active appearance model [53], evidential C-means algorithm proposed in [35], pattern recognition-based method reported in [54] and multi-region-based maxflow algorithm [25]. In our study, the mean DSCs for PZ and CG is 71.15± 4.2%, 70.23±3.4% and 83.01±2.5%, 81.01±3.5% in body-coil images, and 70.2±6.3%, 70.2±6.3% and 83.5±2.5%, 83.5±2.5% in endo-coil images, respectively, which are higher than the 68% and 79% reported by [53], but lower than 75.0±7.0%, 75.0±7.0% and 89.0±3.0%, 89.0±3.0% reported in [24] or 76.0±6.0%, 76.0±6.0% 87.0±4.0%, 87.0±4.0% reported in [35] and 69.1± 6.9%, 69.1±6.9% and 82.2±3.0%, 82.2±3.0% as reported in [25].

However, the methods in [24] and [35] required inputs of 3D multispectral MR images, which included a T_2-w image, a diffusion weighted image and a contrast enhanced MR image. In addition, initialization in both methods required arduous and time-consuming manual organ contouring. In contrast, our proposed method makes use of only a single initialization on T_2w image as the input and requires much less user interactions for initialization.

The automated contours delineation of CG-based on the algorithm proposed in [55] generated a mean DSC of 80% for CG from T_2w MR images without the delineated contours of PZ, which is lower than the DSC result in our study. Litjens *et al.* [24] also mentioned two atlas-based zonal segmentation methods without manual segmentation as initialization that generated the mean DSCs of 57.0±19.0% and 48.0±22% 48.0±22% with respect to PZ contours delineated, which are lower than the reported DSC of PZ contours delineated by the proposed approach. In addition, we conducted similar experiments using the manual segmentation of the whole gland for initialization and validated our proposed method with these initializations using 10 images from the variability testing dataset. The results show a mean DSC of 75.5±6.2%, 75.5±6.2% and 89.2±3.2%, 89.2±3.2% for PZ and CG are comparable to results in [54] and [35]. Although the method proposed by [53] was implemented in C++, in terms of the computational time, it required approximately 200 s to

Table I. Comparison of contour delineation results using Dice coefficient.

	Overall	Base	Apex	Score (Overall)	Score (base)	Score (apex)
DAC and interaction	1.29 ±0.23	0.81 ±0.12	0.82 ±0.05	86.21 ±2.57	88.02 ±4.02	90.02 ±4.45
Method in [56]	0.89 ±0.03	0.84 ±0.06	0.86 ±0.07	85.51 ±3.92	86.98 ±5.21	89.15 ±5.66
Automated DAC	−1.50 ±9.15	−8.31±18.08	−1.03 ±23.97	86.31 ±13.01	87.15 ±7.70	87.55 ±10.37
Method in [57]	0.90 ±0.0	0.86 ±0.12	0.87 ±0.12	87.17 ±2.74	87.05 ±4.21	86.90 ±5.47
Method in [58]	0.87 ±0.03	0.85 ±0.06	0.83 ±0.10	83.17 ±3.53	87.35 ±5.20	86.81 ±7.47
Method in [59]	0.85 ±0.08	0.85 ±0.10	0.77 ±0.23	79.69 ±10.77	87.82 ±8.16	82.13 ±17.39
Method in [60]	0.84 ±0.04	0.84 ±0.06	0.67 ±0.22	78.82 ±5.40	86.62 ±4.90	74.31 ±17.27
Method in [61]	0.83 ±0.06	0.77 ±0.10	0.79 ±0.10	77.46 ±7.61	81.40 ±7.81	84.12 ±7.47

DAC, directional active contours.

segment one 3D prostate MR image, compared with our 180 s CPU implementation Table I. Litjens *et al.* [54] and Makni *et al.* [35] have not reported their computational time. Implementing the proposed algorithm in C++ Mex MATLAB, the computation of cost function will potentially speed up our algorithm. In this regard, the proposed algorithm demonstrates an advantage for CG and PZ contours delineation in terms of accuracy and efficiency. In addition, the low inter-observer and intra-observer variability in VD and CV of the DSC of the proposed method suggests high reproducibility and independence on the observer, which is particularly useful for multi-center clinical trials.

3.5. Comparison with manual contours delineation-based method

Compared with manual contour delineations, our method's DSCs for the base and apex are comparably low and have large standard deviations (86.21 ±2.57 and 88.02 ±4.02 and 90.02 ±4.45%, respectively) because of the low degree of recognition of such a thin structure and complicated by partial volume effects and unclear boundaries between zones. Although segmentation for these two regions is highly challenging even for radiologists, manual post-segmentation surface editing for these regions is still required for the proposed method, introducing approximately 120 s of additional time. However, a DSC of 86.8±5.0%, 81.8± 5.0f̃ or mid-peripheral zone is favorable, which could meet clinical requirements considering values of DSC above 70% are usually regarded as a satisfactory level of agreement between two algorithm. Additionally, the volume measurement results show that our proposed method generated small values for the mean VD for PZ of 2.5 cm_3 in body-coil images and 1.9 cm_3 for endo-coil images. The low inter-observer and intra-observer variability for PZ also indicates a high reproducibility, independent of observers, which is particularly useful for multi-center clinical trials. Moreover, the proposed approach can provide good contours delineation accuracy for all prostate sections of both CG and whole gland, which is highly desirable during image-guided prostate interventions and cancer diagnosis. Note that the PZ surface was obtained by subtracting the CG surface from the whole gland surface. The whole gland and CG surfaces were manually outlined slice-by-slice, which required 8–10 min for each image. In this regard, the computational time of 120 s in addition to approximately 60 s of refinement required by the proposed approach, is preferable for the delineation of the three-zones. Another significant advantage of our algorithm is that it requires much less expertise and workload for radiologists compared with manual contour delineation.

3.6. Accuracy

We present the results for 50 patient datasets using our contours delineation algorithm (see Figure 9). The datasets are split in ten groups and for each patient dataset, we pick one slice for mid-gland section, one for slice base-section and one slice apex-section. For automated contours delineation, many experiments have been conducted in order to fix the good calibration factors with regards to goods DSC values ($\lambda_1 = 0.8$ and $\lambda_2 = 0.5$). In the second step, the good calibration factors are found around $\lambda_2 = 0.45$). In the rest of our experiments, we have used these good calibration

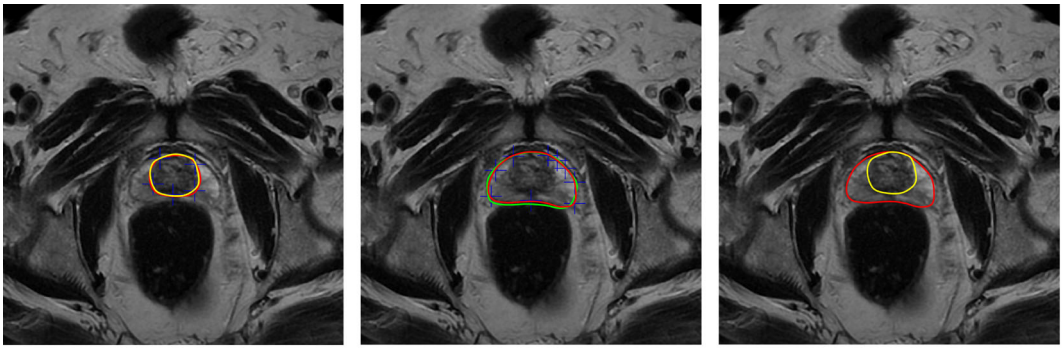

(a) First step of prostate contour delineated (b) placement of control points by the user (c) Correct Prostate contour delineated using DAC with statistical and parametric shape prior model and user feedback

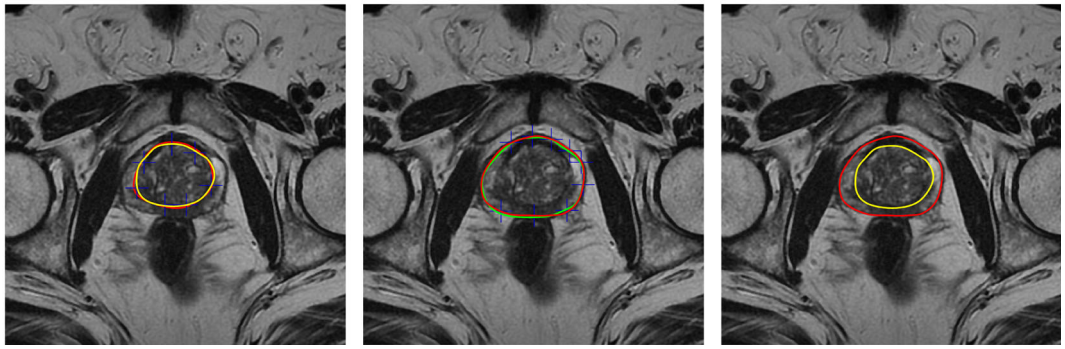

(d) First step of prostate contours delineated, placement of control points by the user in blue color (e) First step of prostate contours delineated, placement of control points by the user in blue color (f) Correct Prostate contour delineated using DAC with statistical and parametric shape prior model and user feedback

Figure 9. Process of prostate contours delineation using directional active contours (DAC) with $\lambda_1 = 0.5$, $\lambda_2 = 0.5$ and $\lambda_3 = 0.1$ in the first stage and $\lambda_1 = 0.1$, $\lambda_2 = 0.1$ and $\lambda_3 = 0.9$ in the second stage. (a) First step of prostate contour delineated; (b) Placement of control points by the user; (c) Correct prostate contour delineated using DAC with statistical and parametric shape prior model and user feedback; (d) First step of prostate contours delineated, placement of control points by the user in blue colour; (e) First step of prostate contours delineated, placement of control points by the user in blue colour; and (f) Correct prostate contour delineated using DAC with statistical and parametric shape prior model and user feedback.

factors. For mid-gland section, the DSC was in average of 81.7±3.3% before user interaction and 93.1±2.3% after user interaction. More specifically, our interactive algorithm is capable to delineate contours for the base-section, mid-section and apex-section of the prostate. We presented the results before and after user intervention. DSC values for the base and apex are comparably low and have large standard deviation (51.3±20.8% and 60.2±14.3%, respectively) because the delineation of prostate region is more challenging even for radiologist using manual contours delineation because of the low degree of recognition of such a thin structure interfered by partial volume effects and unclear boundaries between the whole prostate and others tissues.

3.7. Reproducibility

Ten image datasets were randomly selected for evaluating the reproducibility of the proposed algorithm. For each dataset, we select one image near apex, mid and base of the prostate gland. All datasets are processed four times by the same expert for assessing intra-observer variability in terms of DSC, ABD, HD and RDV. To evaluate the variability introduced by user intervention, 10 images were also delineated by other three blinded users. The proposed method initialized by the three users yielded a mean CV of 0.7%. It can be seen that the proposed method has low variability of both intra-observer and inter-observer contours delineation Tables II–IV.

Table II. Comparison of contours delineation results using average boundary distance.

Methods	Overall	Base	Apex	Score (overall)	Score (base)	Score (apex)
Method in [56]	−1.50 ±9.15	−8.31 ±18.08	−1.03 ±23.97	86.31 ±13.01	87.15 ±7.70	87.55 ±10.37
DAC and interaction	1.3 ±3.2	2.22 ±11.98	1.5 ±33.27	85.27 ±17.83	86.02 ±5.30	86.25 ±11.27
Method in [58]	10.05 ±11.56	7.77 ±22.01	9.59 ±30.51	73.96 ±17.56	86.55 ±11.38	84.60 ±15.29
Method in [59]	12.26 ±17.73	24.75 ±41.69	−7.05 ±39.63	63.49 ±24.70	81.63 ±24.91	81.50 ±20.08
Method in [57]	2.10 ±4.35	5.10 ±20.08	1.03 ±12.17	85.27 ±13.01	86.25 ±6.10	86.78 ±12.42
Automated DAC	−1.50 ±9.15	−8.31 ±18.08	−1.03 ±23.97	86.31 ±13.01	87.15 ±7.70	87.55 ±10.37
Method in [60]	−1.72 ±17.47	5.30 ±25.52	−29.19 ±37.14	71.84 ±21.87	86.46 ±14.29	73.77 ±18.61
Method in [61]	12.62 ±22.25	20.75 ±37.43	0.66 ±28.70	62.15 ±30.81	75.02 ±20.62	85.40 ±12.77

DAC, directional active contours.

Table III. Comparison of contours delineation results using 95% Hausdorff distance.

	Overall	Base	Apex	Score (overall)	Score (base)	Score (apex)
DAC and interaction	1.02 ±2.30	3.02 ±1.21	1.22 ±1.54	87.04 ±3.11	88.59 ±1.19	87.89 ±2.73
Method in [56]	5.54 ±1.74	6.09 ±1.61	4.58 ±1.36	86.35 ±4.28	87.96 ±3.19	87.03 ±3.86
Method in [58]	6.04 ±1.67	5.64 ±2.17	4.60 ±1.39	85.11 ±4.12	88.84 ±4.29	86.96 ±3.94
Automated DAC	4.34 ±3.72	5.12 ±1.23	4.58 ±1.16	84.15 ±3.87	84.90 ±2.23	84.89 ±3.82
Method in [57]	3.34 ±1.12	4.33 ±1.13	3.90 ±1.26	83.075 ±2.35	85.40 ±3.60	85.19 ±4.12
Method in [59]	7.34 ±3.08	6.29 ±3.03	122.28 ±523.16	81.90 ±7.59	87.55 ±6.00	80.72 ±20.05
Method in [60]	7.15 ±2.08	6.12 ±2.14	7.76 ±3.20	82.38 ±5.12	87.89 ±4.22	78.01 ±9.06
Method in [61]	6.72 ±1.42	7.42 ±2.38	5.68 ±1.66	83.43 ±3.51	85.33 ±4.71	83.91 ±4.70

DAC, directional active contours.

Table IV. Comparison of contours delineation results using relative volume differences.

	Relative volume difference					
Methods	Overall	Base	Apex	Score (overall)	Score (base)	Score (apex)
DAC and interaction	1.02 ±2.30	3.02 ±1.21	1.22 ±1.54	87.54 ±3.11	88.96 ±1.19	88.03 ±2.73
Method in [56]	−1.50 ±9.15	−8.31 ±18.08	−1.03 ±23.97	86.31 ±13.01	87.15 ±7.70	87.55±10.37
Automated DAC	5.54 ±5.74	6.09 ±1.61	4.58 ±1.36	84.35 ±4.28	85.96 ±3.19	85.03 ±3.86
Method in [57]	6.70 ±6.70	6.9 ±1.21	5.21 ±2.70	87.20 ±10.28	87.96 ±4.59	86.13 ±7.80
Method in [58]	10.05 ±11.56	7.77 ±22.01	9.59 ±30.51	73.96 ±17.56	86.55 ±11.38	84.60±15.29
Method in [59]	12.26 ±17.73	24.75 ±41.69	−7.05 ±39.63	63.49 ±24.70	81.63 ±24.91	81.50±20.08
Method in [60]	−1.72 ±17.47	5.30 ±25.52	−29.19 ±37.14	71.84 ±21.87	86.46 ±14.29	73.77±18.61
Method in [61]	12.62 ±22.25	20.75 ±37.43	0.66 ±28.70	62.15 ±30.81	75.02 ±20.62	85.40±12.77

DAC, directional active contours.

4. CONCLUSION

In this paper, we have developed and applied a bi-stage interactive contours delineation algorithm as a minimization problem of the DAC model in characteristic function framework without the need of a training shape. We extend the DAC model by incorporating a convex statistical region term to the cost function. First, we applied automatic contours delineation step to the MR image datasets and we model the prostate shape by a parametric deformable ellipse as a shape fitting function to extract the best fitting parameters. In the second step, we introduce the shape fitting function with the best fitting parameters to force the DAC evolution to be close to the prostate shape. User feedback is introduced to adjust iteratively contours position, and the shape fitting parameters are automatically updated. The presented results demonstrate the potential of the proposed method in segmentation of the prostate by DAC and best fitting ellipses. The experimental results on T_2 MR prostate datasets show the effectiveness of the proposed method. Because of the high variability of

the prostate appearance between patients, the non-uniformity of the texture and the lack of clear edge of the prostate apex and base, our method performs poor at certain slice for certain patients; future work will also attempt to overcome these limitations. Because our DAC is implicitly defined in characteristic function framework, an extended 3D version can be performed. Finally, the proposed method provides a fast, accurate and reproducible solution to prostate segmentation from MR datasets. Its reliable performance, combined with minimal user interactions, demonstrates its potential clinical use in guided prostate interventions and computer aided diagnosis of prostate cancer.

REFERENCES

1. Vikal S, Haker S, Tempany C, Fichtinger G. Prostate contouring in mri guided biopsy. 2009; 72594A–72594A–8, DOI: 10.1117/12.812433.
2. Verma S, Bhavsar AS, Donovan J. MR imaging guided prostate biopsy techniques. *Magnetic Resonance Imaging Clinics of North America* 2014; **22**(2):135–144.
3. Quentin M, Blondin D, Arsov C, Schimmöller L, Hiester A, Godehardt E, Albers P, Antoch G, Rabenalt R. Prospective evaluation of mri-guided in-bore prostate biopsy versus systematic transrectal ultrasound (trus)-guided prostate biopsy in biopsy-naïve men with elevated prostate-specific antigen (psa) levels. *The Journal of Urology* 2014; **192**(5):1374–1379. DOI: 10.1016/j.juro.2014.05.090.
4. Sonn GA, Natarajan S, Margolis DJA, MacAiran M, Lieu P, Huang J, Dorey FJ, Marks LS. Targeted biopsy in the detection of prostate cancer using an office based magnetic resonance ultrasound fusion device. *The Journal of Urology* 2013; **189**(1):86–92.
5. Haffner J, Potiron E, Bouyé S, Puech P, Leroy X, Lemaitre L, Villers A. Peripheral zone prostate cancers: location and intraprostatic patterns of spread at histopathology. *The Prostate* 2009; **69**(3):276–282.
6. Villeirs GM, Meerleer GOD. Magnetic resonance imaging (mri) anatomy of the prostate and application of {MRI} in radiotherapy planning. *European Journal of Radiology* 2007; **63**(3):361–368.
7. Ghose S, Oliver A, Marti R, Llado X, Vilanova J, Freixenet J, Mitra J, Sidibe D, Meriaudeau F. A survey of prostate segmentation methodologies in ultrasound, magnetic resonance and computed tomography images. *Computer Methods and Programs in Biomedicine* 2012; **108**(1):262–287.
8. Nguyen K, Sabata B, Jain AK. Prostate cancer grading:gland segmentation and structural features. *Pattern Recognition Letters* 2012; **33**(7):951–961.
9. Mahdavi SS, Chng N, Spadinger I, Morris WJ, Salcudean SE. Semi-automatic segmentation for prostate interventions. *Medical Image Analysis* 2011; **15**(2):226–237.
10. Pallotta S, Bucciolini M, Russo S, Cinzia T, Biti G. Accuracy evaluation of image registration and segmentation tools used in conformal treatment planning of prostate cancer. *Computerized Medical Imaging and Graphics* 2006; **30**(1):1–7.
11. Boydev C, Pasquier D, Derraz F, Peyrodie L, Taleb-Ahmed A, Thiran JP. A comparison of rigid registration methods for prostate localization on cbct and the dependence on rectum distension. *Journal of Physics: Conference Series* 2014; **489**(1):1–6.
12. Gao Y, Zhan Y, Shen D. Incremental learning with selective memory (ilsm): towards fast prostate localization for image guided radiotherapy. *IEEE Transactions on Medical Imaging* 2014; **33**(2):518–534.
13. Mahdavi SS, Spadinger I, Chng N, Salcudean SE, Morris WJ. Semiautomatic segmentation for prostate brachytherapy: dosimetric evaluation. *Brachytherapy* 2013; **12**(1):65–76.
14. Pasquier D, Lacornerie T, Betrouni N, Vermandel M, Rousseau J, Lartigau E. Evaluation dosimetrique d un outil de delineation automatique des organes pelviens a partir d images {IRM} pour la radiothérapie du cancer prostatique. *Cancer/Radiothérapie* 2008; **12**(5):323–330.
15. Sjöberg C, Ahnesjö A. Multi-atlas based segmentation using probabilistic label fusion with adaptive weighting of image similarity measures. *Computer Methods and Programs in Biomedicine* 2013; **110**(3):308–319.
16. Chandra S, Dowling J, Shen KK, Raniga P, Pluim JPW, Greer P, Salvado O, Fripp J. Patient specific prostate segmentation in 3-d magnetic resonance images. *IEEE Transactions on Medical Imaging* 2012; **31**(10):1955–1964.
17. Yang M, Li X, Turkbey B, Choyke P, Yan P. Prostate segmentation in mr images using discriminant boundary features. *IEEE Transactions on Biomedical Engineering* 2013; **60**(2):479–488.
18. Artan Y, Yetik I. Prostate cancer localization using multiparametric mri based on semisupervised techniques with automated seed initialization. *IEEE Transactions on Information Technology in Biomedicine* 2012; **16**(6):1313–1323.
19. Liao S, Gao Y, Lian J, Shen D. Sparse patch-based label propagation for accurate prostate localization in ct images. *IEEE Transactions on Medical Imaging* 2013; **32**(2):419–434.
20. Freedman D, Radke RJ, Zhang T, Jeong Y, Lovelock DM, Chen GTY. Model-based segmentation of medical imagery by matching distributions. *IEEE Transactions on Medical Imaging* 2005; **24**(3):281–292.
21. Ma Z, Tavares JMRS, Jorge RN, Mascarenhas T. A review of algorithms for medical image segmentation and their applications to the female pelvic cavity. *Computer Methods in Biomechanics and Biomedical Engineering* 2010; **13**(2):235–246.
22. Derraz F, Taleb-Ahmed A, Chikh A, Boydev C, Peyrodie L, Forzy G. Segmentation of prostate using interactive finsler active contours and shape prior. *ICISP*, Agadir, Morocco, 2012; 397–405. DOI: 10.1007/978-3-642-31254-0_45.

23. Karasev P, Kolesov I, Fritscher K, Vela P, Mitchell P, Tannenbaum A. Interactive medical image segmentation using pde control of active contours. *IEEE Transactions on Medical Imaging* 2013; **32**(11):2127–2139.
24. Litjens G, Toth R, van de Ven W, Hoeks C, Kerkstra S, van Ginneken B, Vincent G, Guillard G, Birbeck N, Zhang J, Strand R, Malmberg F, Ou Y, Davatzikos C, Kirschner M, Jung F, Yuan J, Qiu W, Gao Q, Edwards PE, Maan B, van der Heijden F, Ghose S, Mitra J, Dowling J, Barratt D, Huisman H, Madabhushi A. Evaluation of prostate segmentation algorithms for mri: The {PROMISE12} challenge. *Medical Image Analysis* 2014; **18**(2):359–373.
25. Qiu W, Yuan J, Ukwatta E, Sun Y, Rajchl M, Fenster A. Dual optimization based prostate zonal segmentation in 3d {MR} images. *Medical Image Analysis* 2014; **18**(4):660–673.
26. Litjens G, Debats O, Barentsz J, Karssemeijer N, Huisman H. Computer-aided detection of prostate cancer in mri. *IEEE Transactions on Medical Imaging* 2014; **33**(5):1083–1092.
27. Hu Y, Carter T, Ahmed H, Emberton M, Allen C, Hawkes D, Barratt D. Modelling prostate motion for data fusion during image-guided interventions. *IEEE Transactions on Medical Imaging* 2011; **30**(11):1887–1900.
28. Niaf E, Rouvière O, Mège-Lechevallier F, Bratan F, Lartizien C. Computer-aided diagnosis of prostate cancer in the peripheral zone using multiparametric mri. *Physics in Medicine and Biology* 2012; **57**(12):3833–3851.
29. Ghose S, Mitra J, Oliver A, Marti R, Llado X, Freixenet J, Vilanova JC, Comet J, Sidibe D, Meriaudeau F. Spectral clustering of shape and probability prior models for automatic prostate segmentation. *Engineering in Medicine and Biology Society (EMBC), 2012 Annual International Conference of the IEEE*, San Diego, California, USA, 2012; 2335–2338. DOI: 10.1109/EMBC.2012.6346431.
30. Liu X, Langer DL, Haider MA, Van der Kwast TH, Evans AJ, Wernick M, Yetik I. Unsupervised segmentation of the prostate using mr images based on level set with a shape prior. *Engineering in Medicine and Biology Society, 2009. EMBC 2009. Annual International Conference of the IEEE*, Minnesota, USA, 2009; 3613–3616. DOI: 10.1109/IEMBS.2009.5333519.
31. Betrouni N, Vermandel M, Pasquier D, Maouche S, Rousseau J. Segmentation of abdominal ultrasound images of the prostate using a priori information and an adapted noise filter. *Computerized Medical Imaging and Graphics* 2005; **29**(1):43–51.
32. Lu C, Chelikani S, Papademetris X, Knisely JP, Milosevic MF, Chen Z, Jaffray DA, Staib LH, Duncan JS. An integrated approach to segmentation and nonrigid registration for application in image-guided pelvic radiotherapy. *Medical Image Analysis* 2011; **15**(5):772–785.
33. Artan Y, Haider MA, Yetik IS. Graph-based active contours using shape priors for prostate segmentation with mri. *IEEE ISBI, 2011*, Chicago, Illonois, USA, 2011; 1459–1462. DOI: 10.1109/ISBI.2011.5872675.
34. Gao Y, Sandhu R, Fichtinger G, Tannenbaum A. A coupled global registration and segmentation framework with application to magnetic resonance prostate imagery. *IEEE Transactions on Medical Imaging* 2010; **29**(10): 1781–1794.
35. Makni N, Betrouni N, Colot O. Introducing spatial neighbourhood in evidential c-means for segmentation of multi-source images: application to prostate multi-parametric {MRI}. *Information Fusion* 2012; **19**(0):61–72.
36. Tsai A, Yezzi A Jr., Willsky AS. Curve evolution implementation of the mumford-shah functional for image segmentation, denoising, interpolation, and magnification. *IEEE Transactions on Image Processing* 2001; **10**(8): 1169–1186.
37. Gong L, Pathak S, Haynor D, Cho P, Kim Y. Parametric shape modeling using deformable superellipses for prostate segmentation. *IEEE Transactions on Medical Imaging* 2004; **23**(3):340–349.
38. Ghose S, Mitra J, Oliver A, Martí R, Lladó X, Freixenet J, Vilanova JC, Comet J, Sidibé D, Meriaudeau F. A mumford-shah functional based variational model with contour, shape and probability prior information for prostate segmentation. In *IAPR International Conference on Pattern Recognition (ICPR)*. IEEE: Tsukuba, Japan, 2012; 121–124.
39. Ghose S, Mitra J, Oliver A, Marti R, Llado X, Freixenet J, Vilanova J C, Sidibe D, Meriaudeau F. A coupled schema of probabilistic atlas and statistical shape and appearance model for 3d prostate segmentation in mr images. *2012 19th IEEE International conference on Image Processing (ICIP)*, Orlando, USA, 2012; 541–544. DOI: 10.1109/ICIP.2012.6466916.
40. Derraz F. Optimal segmentation by fast binary geometric active contours. *Ph.D. Thesis*, Université de Valenciennes Hainaut et Cambresis, 2010.
41. Bresson X, Esedoglu S, Vandergheynst P, Thiran JP, Osher S. Fast global minimization of the active contour/snake model. *Journal of Mathematical Imaging and Vision* 2007; **28**:151–167. DOI: 10.1007/s10851-007-0002-0.
42. Herbulot A, Jehan-Besson S, Duffner S, Barlaud M, Aubert G. Segmentation of vectorial image features using shape gradients and information measures. *Journal of Mathematical Imaging and Vision* 2006; **25**(3):365–386.
43. Lee SM, Abbott AL, Clark NA, Araman PA. Active contours on statistical manifolds and texture segmentation. IEEE *ICIP*, Genova, Italy *(3)*, 2005; 828–831. DOI: 10.1109/ICIP.2005.1530520.
44. Courant R, Friedrichs K, Lewy H. Uber die partiellen differenzengleichungen der mathematischen physik. *Mathematische Annalen* 1928; **100**(1):32–74.
45. Derraz F, Peyrodie L, Taleb-Ahmed A, Forzy G. Texture segmentation using globally active contours model and cauchy-schwarz distance. *2012 3rd International Conference on Image Processing Theory, Tools and Applications (IPTA)*, Istanbul, Turkey, 2012; 391–395. DOI: 10.1109/IPTA.2012.6469562.
46. Michailovich O, Rathi Y, Tannenbaum A. Image segmentation using active contours driven by the bhattacharyya gradient flow. *IEEE Transactions on Image Processing* 2007; **16**(11):2787–2801.
47. Tsybakov A. *Introduction to Nonparametric Estimation*, Springer Series in Statistics. Springer Science+Business Media, LLC: France, 2009.

48. Tutar I, Pathak S, Gong L, Cho P, Wallner K, Kim Y. Semiautomatic 3-d prostate segmentation from trus images using spherical harmonics. *IEEE Transactions on Medical Imaging* 2006; **25**(12):1645–1654.
49. Jehan-Besson S, Barlaud M, Aubert G. Dream2s: deformable regions driven by an eulerian accurate minimization method for image and video segmentation. *International Journal of Computer Vision* 2003; **53**(1):45–70.
50. Klein S, van der Heide UA, Lips IM, van Vulpen M, Staring M, Pluim JPW. Automatic segmentation of the prostate in 3d mr images by atlas matching using localized mutual information. *Medical Physics* 2008; **35**(4):1407–1417.
51. Heimann T, Van Ginneken B, Styner M, Arzhaeva Y, Aurich V, Bauer C, Beck A, Becker C, Beichel R, Bekes G, Bello F, Binnig G, Bischof H, Bornik A, Cashman P, Chi Y, Cordova A, Dawant BM, Fidrich M, Furst JD, Furukawa D, Grenacher L, Hornegger J, Kainmuller D, Kitney R I, Kobatake H, Lamecker H, Lange T, Lee J, Lennon B, Li R, Li S, Meinzer H-P, Nemeth G, Raicu DS, Rau A-M, van Rikxoort EM, Rousson M, Rusko L, Saddi KA, Schmidt G, Seghers D, Shimizu A, Slagmolen P, Sorantin E, Soza G, Susomboon R, Waite JM, Wimmer A, Wolf I. Comparison and evaluation of methods for liver segmentation from ct datasets. *IEEE Transactions on Medical Imaging* 2009; **28**(8):1251–1265.
52. Zou KH, McDermott MP. Higher-moment approaches to approximate interval estimation for a certain intraclass correlation coefficient. *Statistics in Medicine* 1999; **18**(15):2051–2061.
53. Toth R, Ribault J, Gentile J, Sperling D, Madabhushi A. Simultaneous segmentation of prostatic zones using active appearance models with multiple coupled levelsets. *Computer Vision and Image Understanding* 2013; **117**(9): 1051–1060.
54. Litjens G, Debats O, van de Ven W, Karssemeijer N, Huisman H. A pattern recognition approach to zonal segmentation of the prostate on mri. In *Proc. of the 15th Inter. Conf. on MICCAI - Volume Part II*, MICCAI'12. Springer-Verlag: Berlin, Heidelberg, 2012; 413–420. DOI: 10.1007/978-3-642-33418-4_51.
55. Yin Y, Fotin SV, Periaswamy S, Kunz J, Haldankar H, Muradyan N, Turkbey B, Choyke P. Fully automated 3d prostate central gland segmentation in mr images a logismos based approach. 2012; 83143B–83 143B–9.
56. Vincent G, Guillard G, Bowes M. Fully automatic segmentation of the prostate using active appearance models. *Prostate MR Image Segmentation Grand Challenge (PROMISE 12), a MICCAI 2012 Workshop*, Nice, France, 2012.
57. Bernard O, Friboulet D, Thevenaz P, Unser M. Variational b-spline level-set: a linear filtering approach for fast deformable model evolution. *IEEE Transactions on Image Processing* 2009; **18**(6):1179–1191.
58. Birkbecky N, Zhangy J, Requardtz M, Kieferz B, Gallz P, Zhouy SK. Region-specific hierarchical segmentation of mr prostate using discriminative learning. *Prostate MR Image Segmentation Grand Challenge (PROMISE 12), a MICCAI 2012 Workshop*, Nice, France, 2012.
59. Malmberg F, Strand R, Kullberg J, Nordenskjöld R, Bengtsson E. Smart paint a new interactive segmentation method applied to mr prostate segmentation. *Prostate MR Image Segmentation Grand Challenge (PROMISE12), a MICCAI 2012 Workshop*, Nice, France, 2012.
60. Yangming O, Jimit D, Guray E, Christos D. Multi-atlas segmentation of the prostate a zooming process with robust registration and atlas selection. *Prostate MR Image Segmentation Grand Challenge (PROMISE,12), a MICCAI 2012 Workshop*, Nice, France, 2012.
61. Matthias K, Florian J, Stefan W. Automatic prostate segmentation in mr images with a probabilistic active shape model. *Prostate MR Image Segmentation Grand Challenge (PROMISE 12), a MICCAI 2012 Workshop*, Nice, France, 2012.